Accelerated Acoustic Boundary Element Method and the Noise Generation of an Idealized School of Fish

Nathan Wagenhoffer, Keith W. Moored, and Justin W. Jaworski

Lehigh University, Bethlehem PA 18015, USA,
nate@lehigh.edu

Abstract. A transient, two-dimensional acoustic boundary element solver is developed using double-layer potentials accelerated by the fast multiple method for application to multibody, external field problems. The formulation is validated numerically against canonical radiation and scattering configurations of single and multiple bodies, and special attention is given to assessing model error. The acoustic framework is applied to model the vortex sound generation of schooling fish encountering 2S and 2P classes of vortex streets. Vortex streets of fixed identity are moved rectilinearly in a quiescent fluid past representative schools of two-dimensional fish, which are composed of four stationary NACA0012 airfoils arranged in a diamond pattern. The induced velocity on the fish-like bodies determines the time-dependent input boundary condition for the acoustic method to compute the sound observed in the acoustic far field. The resulting vortex noise is examined as a function of Strouhal number, where a maximum acoustic intensity is found for $St \approx 0.2$, and an acoustic intensity plateau is observed for swimmers in the range of $0.3 < St < 0.4$. In the absence of background mean flow effects, numerical results further suggest that the value of Strouhal number can shift the acoustic directivity of an idealized school in a vortex wake to radiate noise in either upstream or downstream directions, which may have implications for the the study of predator-prey acoustic field interactions and the design of quiet bio-inspired underwater devices.

1 Overview

Animal collectives such as schools of fish can generate flow-induced noise from the wake production of individuals members and by the scattering of these wakes by their neighbors [5,13]. Hydrodynamic locomotion of fish for engineering applications continues to attract attention [7,14,18,21], while the literature on flow-induced noise generation by fish and fish schools remains relatively unexplored. In contrast, many techniques exist to estimate the scattered acoustic field off of a fish school produced by a prescribed pulse, primarily for determining its population size [1,6,13,20]. The distinct approach here seeks to estimate the hydrodynamic self-noise due to vorticity production of single swimmers and swimming collectives. An improved understanding of the noise generation of fish may enable strategies to mimic the vortex self-noise signature of an animal in an underwater vehicle(s). Alternatively, an improved understanding of fish noise signatures may help detect and distinguish bio-robotic underwater vehicles from their biological counterparts.

The reduction of this complex physical problem, involving acoustic interactions among multiple bodies, to a predictive numerical model requires a rapid framework to assess multiple configurations efficiently. To this end, a transient, two-dimensional acoustic boundary element method (BEM) is developed to solve for the acoustic field resulting from a vortical field or distribution of acoustic sources scattered by the solid bodies in a collective. To accelerate this numerical framework, the boundary element solution and subsequent evaluation of the resulting acoustic field are computed with the fast multipole method [22]. This method reduces the computational cost of the boundary element solution in two spatial dimensions from $O(n^2)$ to $O(n \log n)$ for n elements and is accompanied by a large reduction in memory cost [16], which would otherwise hamper the boundary element approach in the case of many elements and/or bodies, as well as future extensions to three spatial dimensions. To effect a transient solution, the acoustic solver aggregates individual frequency-domain solutions to produce a time-domain solution using the convolution quadrature method [10,17]. The present study implements distributions of Gaussian cores with fixed identity and prescribed movement to represent the vortical field and its transient interactions with nearby solid bodies [15]. The induced velocity of the vortical field is then fed forward into the boundary element solver to produce the acoustic field. The novelty of the acoustical numerical framework presented lies in the development and implementation of a transient double-layer potential accelerated by the fast multipole method.

The present work outlines the development, validation, and application of a transient, two-dimensional, acoustic boundary element solver to multibody, external field problems, including application to a model

school of fish. Section 2 details the acoustic boundary element formulation with a double-layer potential and its acceleration via the fast multipole method. Section 3 validates the numerical method against a canonical scattering configuration with an analytical solution and further demonstrates the capability of the method to handle multiple scatterers and transient forcing. Section 4 applies the acoustic framework to a model fish schooling arrangement encountering $2S$ and $2P$ classes of vortex streets and examines the resulting vortex noise as a function of Strouhal number. Concluding remarks from this study are made in §5.

2 Boundary element method

The propagation of linear waves through domain $\mathcal{V}$ with a boundary S_b is described by the non-dimensional wave equation:

$$\begin{aligned} \partial_t^2 p - \nabla^2 p = 0 \quad \text{in} \quad \mathcal{V}, \\ p(\mathbf{x}, t=0) = \partial_t p(\mathbf{x}, t=0) = 0, \\ p = g(t) \quad \text{on} \quad S_b, \end{aligned} \tag{1}$$

where $\mathbf{x}$ is the position in the exterior domain $\mathcal{V}$, t is time, g is some prescribed forcing function on the boundary, and p is the acoustic pressure. The combination of the Green's function solution to the wave equation in an infinite domain with Green's second identity yields a general solution for the pressure field external to a body or a set of bodies expressed as a boundary integral equation [12]:

$$p(\mathbf{x}, t) = \int_0^t \left[\int_{S_b} m(\mathbf{x} - \mathbf{x}', t-\tau)\eta(\mathbf{x}', \tau) dS_b - \int_{S_b} l(\mathbf{x} - \mathbf{x}', t-\tau) \frac{\partial \eta}{\partial n}(\mathbf{x}', \tau) dS_b \right] d\tau, \quad t \in [0, T]. \tag{2}$$

Here η is the vector potential associated with a single-layer potential, and the normal derivative, $\partial\eta/\partial n$, is associated with the double-layer potential, m and l are respectively single and double-layer retarded time potential operators, $\mathbf{x}'$ is a source point, $\hat{n}$ is the outward normal of the body surface, and τ is a temporal dummy variable.

The substitution of boundary condition (1) into the fundamental solution (2) produces the time-varying boundary value problem,

$$\int_0^t \left[\int_\Gamma m(\mathbf{x} - \mathbf{x}', t-\tau)\eta(\mathbf{y}, \tau) dS_b - \int_{S_b} l(\mathbf{x} - \mathbf{y}, t-\tau) \frac{\partial \eta}{\partial n}(\mathbf{y}, \tau) dS_b \right] d\tau = g(t), \quad \mathbf{x} \in S_b, \tag{3}$$

which is to be solved by the boundary element method. For the two-dimensional wave equation, the fundamental solutions of the single-layer and double-layer potentials are

$$M(\mathbf{r}, \kappa) = \frac{i H_0^{(1)}(\kappa r)}{4}, \tag{4}$$

$$L(\mathbf{r}, \kappa) = \frac{i\kappa H_1^{(1)}(\kappa r)}{4} \frac{\mathbf{n} \cdot \mathbf{r}}{r}, \tag{5}$$

where $H_n^{(1)}$ are Hankel functions of the first kind of order n. The operators M and L, are Laplace transforms of the retarded-time potentials, m and l. Here $\mathbf{r} = \mathbf{x} - \mathbf{x}'$, is position vector from a source to an observer, $r = |\mathbf{r}|$, and κ is the wavenumber. The frequency-domain potential operators (4) and (5) are used by the convolution quadrature method [10] to generate a time-stepping procedure to solve (3).

Imposing a velocity on the boundary, the frequency-domain double-layer indirect formulation of (3) becomes

$$\left(-\frac{1}{2} I + L'(\mathbf{r}, \kappa) \right) \eta = -\mathbf{V}_\mathrm{i}, \tag{6}$$

$$P_\mathrm{field} = L_\mathrm{field}(\mathbf{r}, \kappa)\eta, \tag{7}$$

where I is the identity matrix, $\mathbf{V}_\mathrm{i}$ is the incident velocity on the boundary, L' is the adjoint of the double-layer operator using the outward normal at the observation point instead of the normal of the source, and P_field is the pressure at an observation point in the field.

2.1 Time discretization

The retarded-time potential operators found in (2) are evaluated as convolution integrals. The Laplace transforms of the single-layer and double-layer potential operators, (4) and (5), respectively, are convolved with an associated potential field. The potential field is evaluated by a convolution quadrature. The quadrature has an associated weight that is defined by a power series. This methodology of time discretization can be achieved via a convolution quadrature method put forth by Lubich [17]:

$$V\frac{\partial \Phi}{\partial t} = \int_0^t v(t-\tau)\phi(\tau)d\tau.$$

Here V represents a Laplace transform of the v operator, a characteristic differential operator of the transient wave equation, and ϕ is some known potential distribution. The interested reader can look to [10] for a detailed explanation of the convolution quadrature method. For problems with a form similar to (3), the retarded-time operator is a convolution that can be discretized as

$$v(\mathbf{x}, t-\tau)\phi(\tau) = \int_0^t V(\mathbf{x}-\mathbf{x}', t-\tau)\phi(\tau)d\tau. \tag{8}$$

Splitting the time domain into $N+1$ time steps of equal spacing, $\Delta t = T/N$ and $t_n = n\Delta t$ for $n = [0, 1, ..., N]$, the discrete convolution can be viewed as a sum of weights of the V operator at discrete times of ϕ:

$$V\frac{\partial \Phi(t_n)}{\partial t}^{\Delta t} = \sum_{j=0}^{n} \omega_{n-j}^{\Delta t}(V)\phi^{\Delta t}(t_j), \tag{9}$$

where the superscript Δt indicates the weight for a specific time-step size. The series expansion can be arranged to solve for the convolution weights, ω:

$$V\left(\frac{\gamma(\zeta)}{\Delta t}\right) = \sum_{n=0}^{\infty} \omega_{n-j}^{\Delta t}\zeta^n, \quad |\zeta| < 1, \tag{10}$$

$$\omega_{n-j}^{\Delta t} = \frac{1}{2\pi i}\oint_C \frac{V(\frac{\gamma(\zeta)}{\Delta t})}{\zeta^{j+1}}d\zeta, \tag{11}$$

where C is a circle of radius $0 < \lambda < 1$ centered at the origin. A second-order backwards difference function, $\gamma(\zeta) = (1-\zeta) + \frac{1}{2}(1-\zeta)^2$, is used to define the spacing of the integration. A review of other integration methods that can be incorporated into the convolution quadrature method is presented in [10]. Employing a scaled inverse transform, the weights become

$$\omega_{n-j}^{\Delta t,\lambda}(V) = \frac{\lambda^{-j}}{N+1}\sum_{l=0}^{N} V(s_l)\zeta_{N+1}^{lj}, \tag{12}$$

with

$$\zeta_{N+1} = \exp\left(\frac{2\pi i}{N+1}\right) \tag{13}$$

being the temporal quadrature spacing, and

$$s_l = \gamma(\lambda\zeta_{N+1}^{-l})/\Delta t \tag{14}$$

is the accompanying time dependent complex wavenumber that is generated. The value of s_l is different for each time step and provides the link between the frequency-domain solver and a transient boundary integral equation such as (3). For this formulation, $\lambda = \Delta t^{3/N}$ is selected based on the error analysis of Banjai and Sauter [2].

Placing (12) into the boundary value problem (3) yields

$$\frac{\lambda^{-j}}{N+1}\sum_{l=0}^{N} M(s_l, \mathbf{x})\hat{\eta}_l(\mathbf{x})\zeta_{N+1}^{lj} = \frac{\lambda^{-j}}{N+1}\sum_{l=0}^{N} \hat{g}_l\zeta_{N=1}^{lj} \tag{15}$$

for a double-layer boundary representation. Here g_n is a discrete representation of the boundary conditions. This transformation can be applied to other potential distributions, such as the double-layer potential, in the same manner. The inverse of the convolution transform of (12) is

$$\hat{\phi}_l = \sum_{j=0}^{N} \lambda^j \phi_j^{\lambda} \xi_{N+1}^{-lj}. \tag{16}$$

By applying a discrete Fourier transform to (16), a system of $N+1$ equations is generated:

$$K(s_l, \mathbf{x})\hat{\eta}_l(\mathbf{x}) = \hat{g}_l(\mathbf{x}). \tag{17}$$

The convolution quadrature method [2] is employed to discretize the wave problem into a system of wave equations that are uncoupled in time. This discretization allows one to solve $N+1$ independent problems in the frequency domain using wavenumbers that are generated via the convolution quadrature method. The time-domain solution is recovered by applying the inverse Fourier transform (16).

The convolution quadrature method is applied to (3) and a velocity-based boundary condition is applied. This approach allows the use of the indirect Neumann condition double-layer formulation seen in (6), which then is used to define the test problems presented in §3.

2.2 Spatial discretization

The boundaries of noise-scattering bodies are discretized here using equal-length line elements. The boundary condition for the problem represented by the boundary integral equation (3) is enforced at collocation points located at the midpoint of each element. The boundary elements are constant strength elements in the current study, but Gaussian quadrature elements could also be easily implemented by evaluating the integration points as collocation points and summing the products with the appropriate weights for each element [12].

2.3 Fast multipole method

The boundary element system (17) creates a dense influence matrix when a direct calculation is performed at each time step. Therefore, the total number of operations is $O(Nn^2)$, where N is the total number of time steps and n is the number of boundary elements. The fast multipole method (FMM) put forth by Rohklin and Greengard [9,22] reduces the order of operations needed to solve these types of systems to $O(Nn \log n)$.

The reduction in computational effort is achieved by embedding the FMM into an iterative linear equation solver. Figure 1 compares the computational speed of a direct solution of boundary values against its FMM counterpart. This embedded approach removes the calculation of the dense matrix and associated linear solve with a series of FMM calculations. FMM2DLIB is an open-source version of the FMM that was implemented due to its easy implementation and multi-core optimization [8]. The FMMLIB2D library evaluates the potential field due to particle sources governed by the Helmholtz equation in free space.

The FMM consists of several steps that make it an efficient algorithm for matrix-vector multiplication to find a potential ϕ of the form

$$\phi(x_j) = \frac{i}{4} \sum_{k=0}^{N} \phi(x_k) H_0^1(s_l|x_j - x_k|) + \frac{\partial \phi(x_k)}{\partial n} H_1^1(s_l|x_j - x_k|) \frac{\kappa n_k (x_k - x_k)}{|x_j - x_k|}.$$

There are three main operations to making the FMM-BEM work. The first is an implementation of a quad-tree structure onto the domain. The second is the definition of translation operators that are used to relate different nodes of the quad-tree to each other. Finally, the FMM is coupled with an iterative linear solver (e.g. bi-conjugate gradient, generalized minimal residual, etc.) to determine the strength of each element. The generalized minimal residual (GMRES method) [23] is an iterative scheme to compute the solution of a system of linear equations that approximates the solution by finding the vector that produces a minimal residual error.At each iteration of GMRES, the FMM accelerates a matrix-vector multiplication used to evaluate the convergence criteria of that iteration. The natural fit of FMM into a GMRES solver is the main reason why this particular linear solver was selected. The GMRES, with a tolerance of 10^{-5}, is employed here to solve (17).

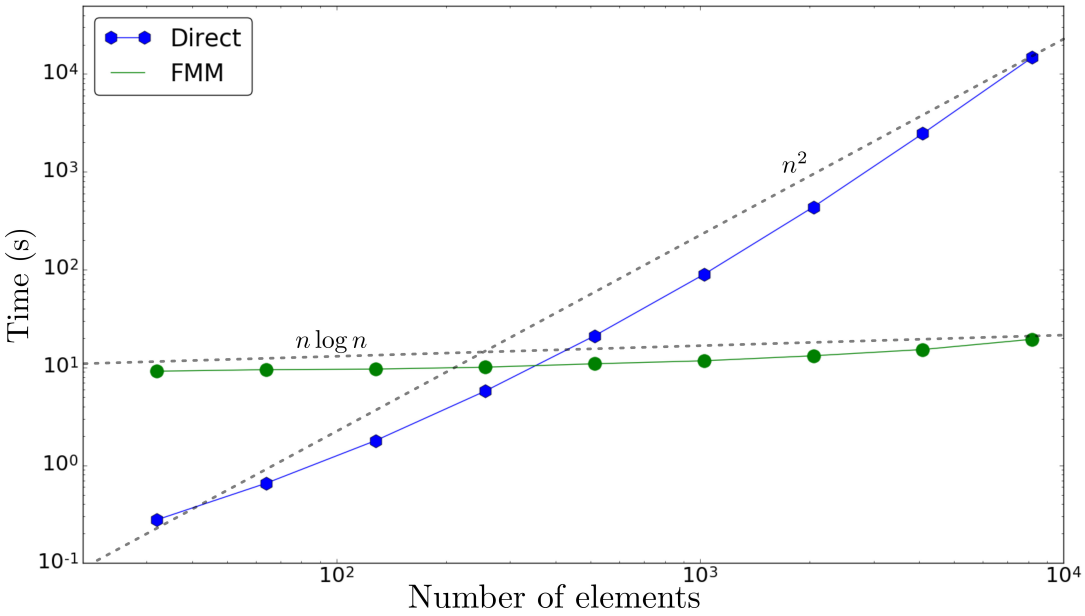

Fig. 1. Comparison of a direct computation with its FMM counterpart for an increasing number of boundary elements. The system used was set to T=1 with 100 time steps. A field of 256 points was evaluated at each time step.

The discrete geometry is recursively subdivided by placing it into a quad-tree structure. The quad-tree structure is constructed such that the quad-tree will descend to a set number of branches. Figure 2 shows the descent of a branch of an arbitrarily sized quad-tree with four levels. Once the data structure is developed, the calculation of the method begins with the 'upward pass'. A weighted summation of the elemental potential strengths is computed into a moment at each terminal node. The moments of four children nodes are translated up to the parent node. The upward translation process occurs until the level before the tree's root. Now each of the top four nodes contain the translated values of the potentials of their children nodes in a single value. The values at this level are in effect a representation of how the local nodes influence each other at each level in the quad-tree structure. The next step is to then cascade these values back down into the tree structure. The 'downward pass' step passes the moments down the tree structure. The 'downward pass' is calculated over nodes with adjacent but distinct parents and is performed to the terminal node. The value that is passed into the terminal nodes is then translated to all of the elements in the node. The prior steps define the far-field interaction between elements. The potential of all elements found in a terminal node are deemed to be in the near field. The potentials of near field elements are directly evaluated. The near field is defined by the tolerance set. For a low error tolerance, the near field contains more elements. The use of these steps approximates far-field interactions and thus a full matrix is not built for a matrix-vector multiplication. Note that here the near-field and far-field designators in this section refer to the relationship between elements placements in the quad-tree structure and not the acoustic near field or far field.

The translation operators necessary to pass information from source points to a far-field observer are defined as multipole-to-multipole, multipole-to-local, and local-to-local, which are respectively shortened to M2M, M2L, and L2L. All of these translation operators make use of an initial moment summation that needs to be calculated only once. The GMRES solver is set to an error that is found to be less than the model error and should therefore not impact the accuracy of the results [23].

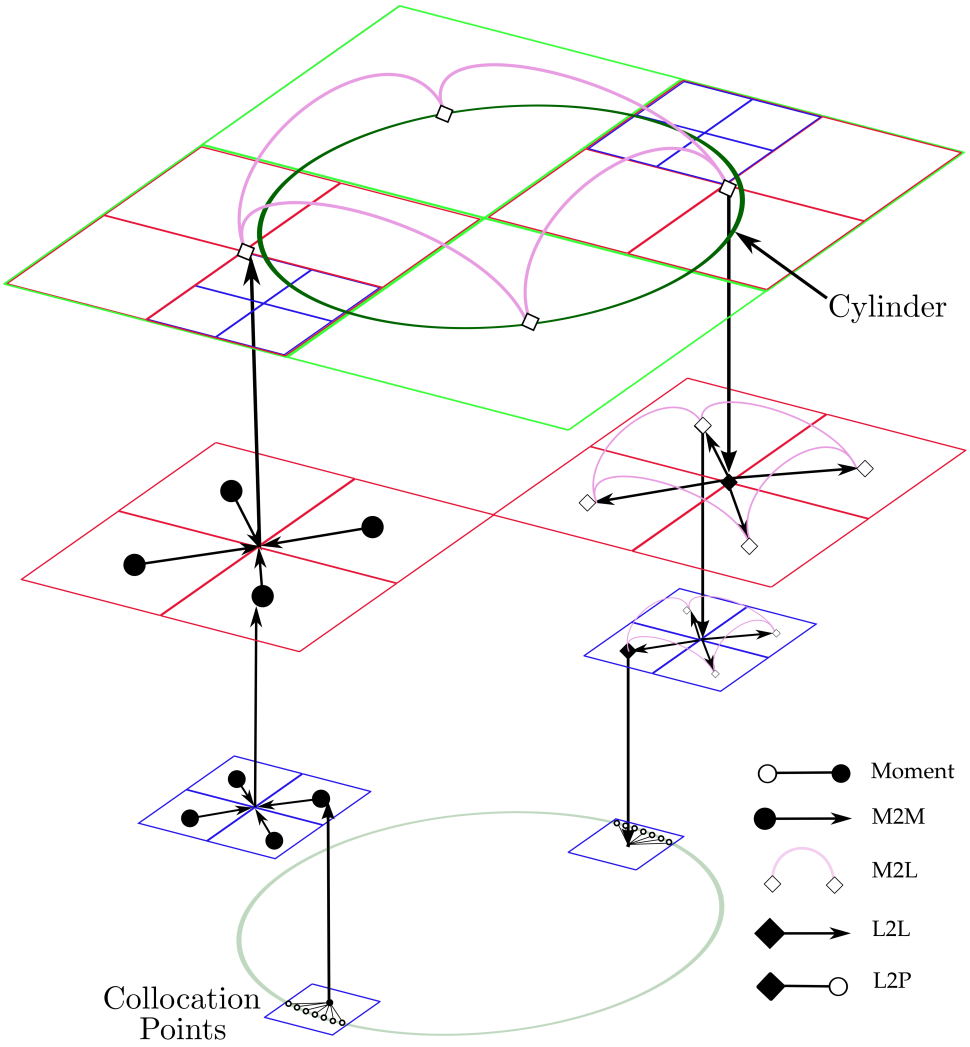

Fig. 2. Schematic of information transfer of the fast multipole method using a partial quad-tree structure. Small green circles represent the collocation points of a discretized cylinder. The entire domain is recursively divided into smaller and smaller squares, shown here as green, red, and then blue in decreasing size. The above quad-tree shows a four-level tree. The depiction shows only a simplified version of the actual FMM, representing the contribution of one far-field terminal leaf on the potential values at another terminal leaf.

The translation and moments for the two-dimensional frequency domain problem are summarized in Lui [16] and are reproduced here:

$$\text{Moment}: M_n(y^*) = \frac{i}{4}\int_{\mathcal{S}} i^n J_n(s_l(y-y^*))\eta(y)d\Gamma(y)e^{in\alpha}, \tag{18}$$

$$\text{M2M}: M_n(y') = \sum_{m=-\infty}^{\infty} I_{n-m}(y-y')M_m(y), \tag{19}$$

$$\text{M2L}: L_n(x) = \sum_{m=-\infty}^{\infty} (-1)^m O_{n-m}(x-y)M_m(y), \tag{20}$$

$$\text{L2L}: L_n(x^*) = \sum_{m=-\infty}^{\infty} I_m(x^*-y)L_{n-m}(x^*). \tag{21}$$

Here α is the angle from the source point to the center of the leaf at the terminus of the quad-tree, s_l is the wavenumber associated with each independent time step, and $O_n(\mathbf{x}) = i^n H_n^{(1)}(s_l r)\exp(in\alpha)$ and $I_n = (-i)^n J_n(s_l r)\exp(in\alpha)$ are auxiliary functions that translate the influence of the multipole potentials over a distance r at angle α. In the auxiliary functions, J_n is a Bessel function of the first kind of order n.

The fast multipole frequency domain operators (18-21) are sufficient for the present study, as the convolution quadrature method transforms the time-domain problem into sets of frequency-domain problems. The quad-tree structure will remain constant at each time step, as the domain contains a static rigid body or bodies in the scenarios considered in this work.

3 Validation and demonstration

This section presents the capability of the transient acoustic BEM to accurately simulate vortex-solid or acoustic-solid interactions in single- and multi-body scenarios. A validation case of plane wave scattering on a cylinder establishes the temporal and spatial model errors. The validation case is extended to include multiple bodies to demonstrate how the model can compute many degrees of freedom rapidly and with with the same order of error as the single scatterer study. A qualitative demonstration of a soliton wave impinging onto an irregular arrangement of cylinders shows the capability of the solver to model the interactions between scattering bodies. Each of the validation cases were selected to ensure that the method is suitable for modeling noise generation due to wake-body interactions in an idealized school of fish. The plane wave scattering study §3.1 demonstrates the capability of the solver to model wake-body interactions and establishes the model error. The multiple-scatterer study §3.2 demonstrates that there is no loss in model error when multiple body interactions are introduced. Finally, the capability of the method to define transient acoustic interactions between multiple bodies is demonstrated in §3.3.

The accuracy of the BEM is measured by the absolute error in the acoustic field since exact boundary potential values are not readily available for all of the validation cases considered. The error is determined at 25 points in the acoustic field at locations shown in figure 4. The L_2 norm is used to show the relative error between the numerical and the analytic values at each time step. The maximum of these L_2 values for all simulated time is designated as the error.

$$E_{L_2} = \max_{t\in T}\left(\frac{\sqrt{\sum_x |P_{\text{exact}}(\mathbf{x},t) - P_{\text{BEM}}(\mathbf{x},t)|^2}}{\sqrt{\sum_x |P_{\text{exact}}(\mathbf{x},t)|^2}}\right) \tag{22}$$

The numerical problem is rendered dimensionless by using bulk modulus ρc^2, radiator diameter $2a$, and parameter $2a/c$ as the pressure, length, and time scales, respectively, where ρ is the fluid density and c is the speed of sound.

3.1 Plane wave scatterers

The capability of the method to model acoustic scattering by a solid body is now demonstrated and validated. Figure 3 illustrates the model of a rigid circle of radius a placed at the origin that is bombarded by a harmonic field of plane waves. The incident field of unit strength has the form

$$P_{\text{i}}(x,t) = \exp[i(\kappa r\cos\theta - \omega t)],$$

where ω is the angular frequency, κ is the wavenumber, and $x = r\cos\theta$. The analytical result for the scattered field is [11]

$$P_{\mathrm{s}}(x,t) = e^{i\omega t}\sum_{n=0}^{\infty}\epsilon_n i^n\left[J_n(\kappa a) - \frac{J_n'(\kappa a)H_n(\kappa r)}{H_n'(\kappa a)}\cos n\theta\right]. \tag{23}$$

The total acoustic field is the sum of the incident and scattered fields, $P_{\mathrm{t}} = P_{\mathrm{s}} + P_{\mathrm{i}}$.

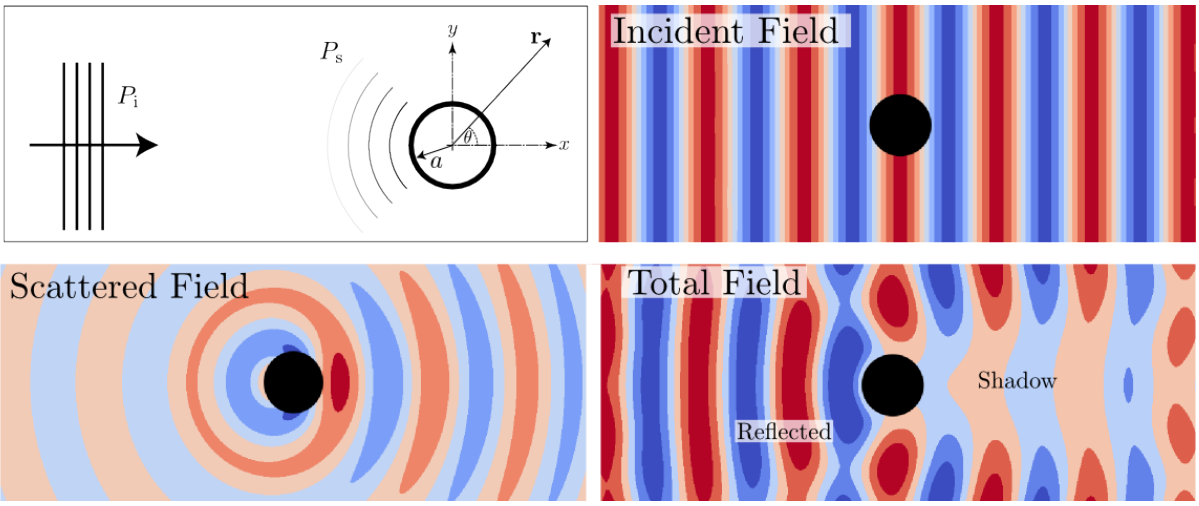

Fig. 3. Schematic of a harmonic plane wave, P_{i} impinging upon a rigid cylinder of radius a, to produce scattered field P_{s}. The total field is the linear superposition of the incident field and the scattered wave, which includes a reflected wave region ahead of the cylinder and a shadow region behind the body.

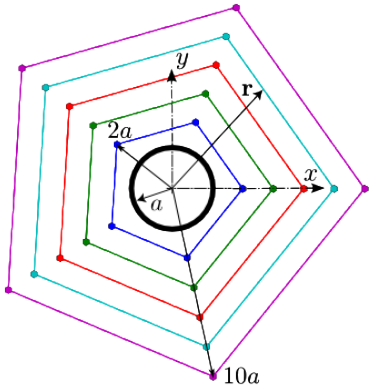

Fig. 4. Schematic of the arrangement of observation points used to evaluate error. Not drawn to scale.

The interaction of the harmonic incident field with the solid cylinder is as follows. The incoming plane waves propagate in the positive x-direction and make initial contact with the cylinder at $(r,\theta) = (a,\pi)$. In the area in front of the cylinder, the plane waves are reflected back onto themselves. The waves reflect at the front of the cylinder to create a shadow region aft of the body. The length of the shadow region is dictated by the wavenumber, with larger values resulting in a smaller shadow region. An annular grid of 25 observation points shown in figure 4 are used to sample all of the regions of the scattered field and determine the L_2 error norm.

Figure 5 compares the transient acoustic response at a point in the acoustic field to the analytical solution to harmonic wave forcing. Here $\omega = 1$, $\kappa = 2$, and arbitrary point $(r,\theta) = (5, \frac{\pi}{9})$ are selected for

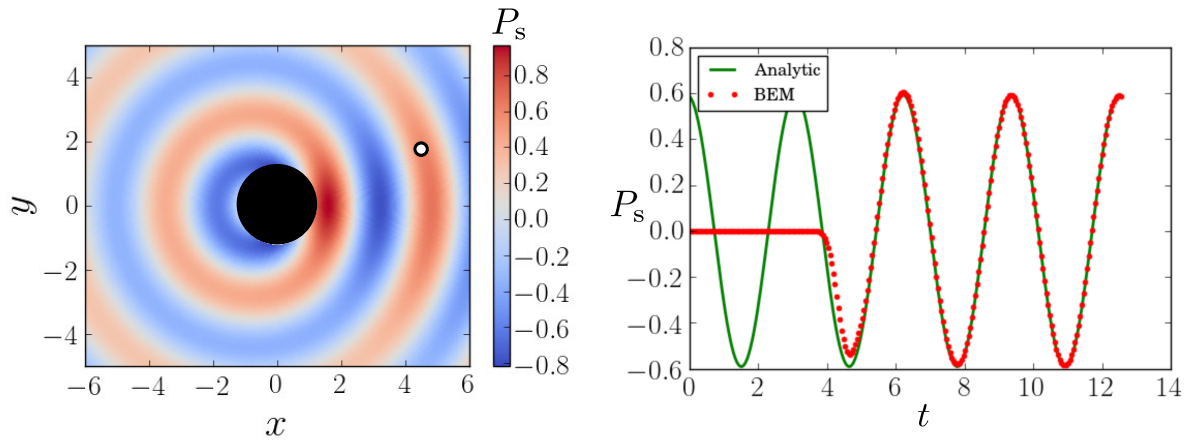

Fig. 5. A comparison of the analytical to BEM results of the plane wave scatterer study. The image on the left shows the fully developed scattered field. The observation point, denoted by a black circle in the left image, is placed at the arbitrary point $(r, \theta) = (5, \frac{\pi}{9})$. The right image compares the time history of the scattered field at the observation point. $\omega = 1$ and $\kappa = 2$.

this example. Note the absence of a signal in the BEM solution until the initial scattered wave reaches the observation point, after which the numerical solution quickly converges to the analytical result.

Temporal and spatial discretization independence of the numerical solution are shown in figure 6 for the indirect double-layer formulation (6). For the spatial convergence study, a period of $T = 4\pi$ is divided into 256 equidistant time-steps. An increasing number of elements on the boundary were used to compare the BEM solution with (23). The temporal convergence study (figure 6-b) had a boundary of 1024 equal length elements over a total period of $T = 4\pi$. The total period is divided into increasing numbers of equidistant time steps. Spatial convergence occurs at approximately 512 elements, showing a relative error of less than 0.1% when using more than 256 time steps.

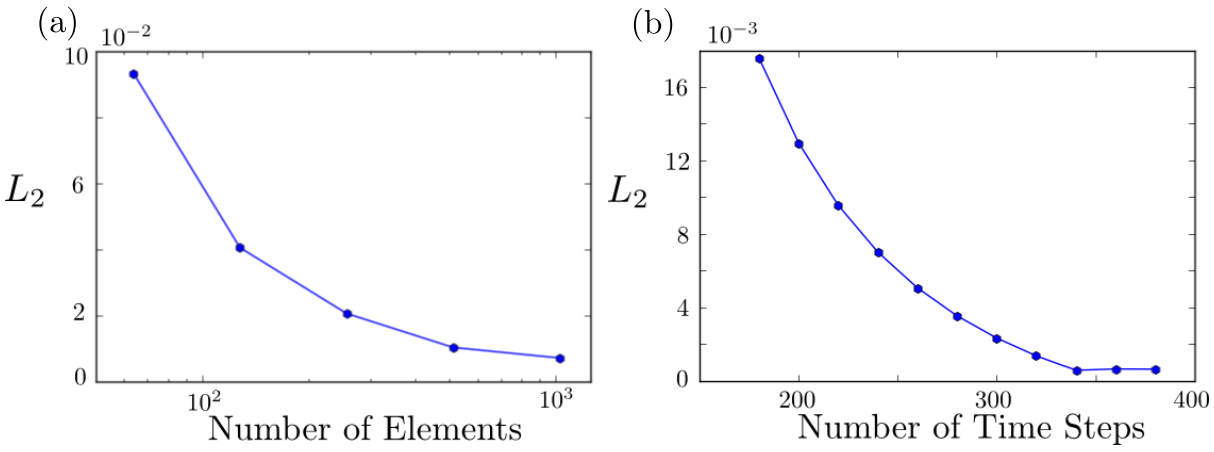

Fig. 6. Spatial and temporal convergence of the indirect double-layer formulation for a single scatterer. The sample of 25 points in the field is compared to the analytic solution of the plane wave case for this spatial convergence study. The L_2 norm is calculated at time steps after the field becomes fully developed at the observation location.

3.2 Multiple scatterers

To underscore the capabilities of an FMM-accelerated BEM solver, a problem involving many degrees of freedom is now proposed. The model problem consists of a ring of cylinders arranged into a circular pattern that is bombarded impinged by a plane wave from the acoustic far field. If the spacing between cylinders is sufficiently small and the ring is acoustically compact, then the resulting scattered field will

be qualitatively similar to the plane wave study of §3.1. A spatial convergence study is performed across the scattered field in a manner similar to §3.1.

The ring of cylinders is composed of 36 cylinders each with a radius of $a/20$, as shown in the schematic of figure 7. The vertical and horizontal spacing between cylinders is the same as the radius of the individual cylinders. The radius of the system of cylinders is approximately unity, $a \approx 1$. The indirect double-layer distribution defined by (6) is used to find the boundary strengths. Table 1 shows system convergence of relative error, where a reference case of 16,384 elements per cylinder was used to compute the L_2 norm. The multibody system requires considerably more elements to reach convergence than the simple scatterer of §3.1. This increase in resolution should be expected, as the boundary must account for the interaction of a cylinder with the incoming wave in addition to the scattered fields of the other cylinders. The total time period of the simulation is $\mathrm{T} = 8\pi$ and is discretized into 128 equally spaced time steps. The acoustic field calculation is performed over the annular grid found in figure 4. All of the time calculations include the field evaluation step. The evolution of the acoustic field for the multiple scatters can be seen in figure 7. The given wave speed and radial dimension of the multiple scatterers is $\kappa a = 2$, resulting in a scattered field similar to that of figure 5. The interior of the ring of cylinders can be observed as the spacing of the system allows the plane wave to penetrate this area. A comparison of the scattered acoustic field with the analytic solution (23) of a single scatterer is shown in figure 7.

Elements per cylinder	Total Elements	L_2 norm	Time(s)
128	3968	0.909	108
256	7936	0.498	155
512	15872	0.285	256
1024	31744	0.149	478
2048	63488	0.079	802
4096	126976	0.035	1642
8192	253952	0.012	3047
16384	507904	reference	5889

Table 1. A ring of 36 cylinders is bombarded by an incoming plane wave. The simulation has to have 128 time steps over a period of 8π, and the number of elements doubles for each successive simulation. The most resolved system is designated the reference solution to compute the relative L_2 error for the less resolved cases. Each simulation was computed with an Intel® Core™ i7-4930K CPU @ 3.40GHz with 64 GB of RAM.

3.3 Transient multibody scattering

Figure 8 depicts a system with four cylinders designed to illustrate the transient interactions among multiple bodies. A single soliton wave is used for transient acoustic forcing instead of a harmonic field. The wave has a form

$$P_{\mathrm{i}} = 2\sin(\omega(t-x))\sin(\omega\lambda)\exp\left(-\left[\frac{t-x}{\lambda^2}\right]^2\right)/\lambda^2,$$

where λ is the wavelength. The radius of the scatterers is equal to λ for the configuration shown in the schematic of figure 8. The soliton wave has a single interaction with each rigid body, whose scattered field then interacts with neighboring scatterers. Figure 8 illustrates the interactions between four irregularly-placed rigid bodies. Primary scattering off of the two left-most bodies can be seen in images (a→ d). By image (g), secondary scattering can be observed near the left-most body. The scattered waves continue to reflect off of the other cylinders as the incoming wave completes its movement across the arrangement of cylinders.

4 Noise production of a small idealized fish school

The validation of the acoustic solver in §3 enables the investigation of vortex sound generated by prescribed wakes interacting with fish, modeled as two-dimensional rigid foils. The noise generation of swimming schools of fish has historically received little attention due to the challenges associated with recording reliable sound from specific species and the low amplitude noise associated with fish locomotion [5]. Presented here is an approximation of the scattered noise due to interaction with the wake from

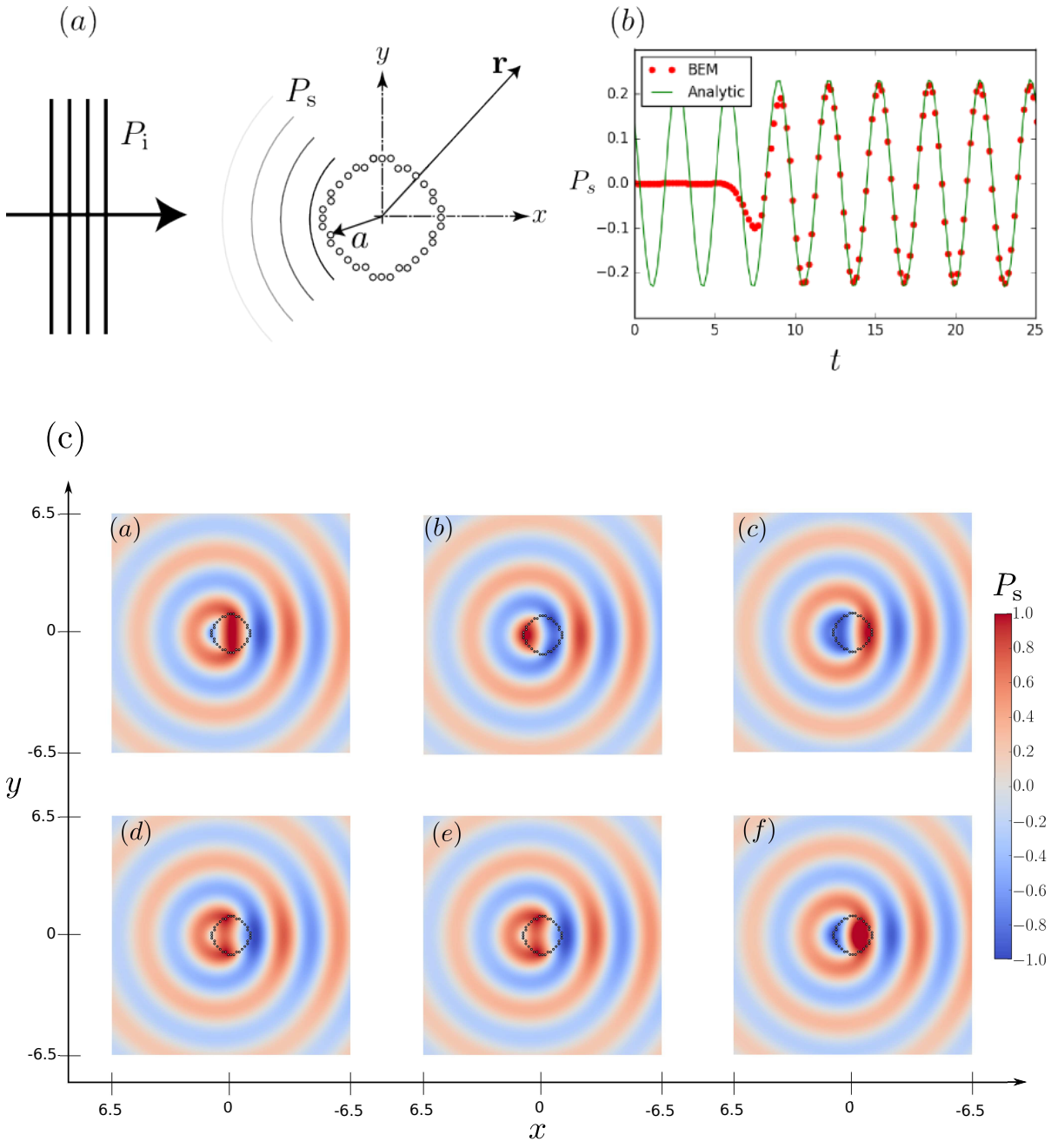

Fig. 7. Image (a) shows a schematic of the multiple-scatterer problem. Image (b) is a comparison of (23) with the BEM scattered field of multiple bodies at arbitrary observation point $(r,\theta) = (9.2,\frac{\pi}{4})$. After two periods, the scattered wave reaches the observation point and good qualitative agreement is seen. Image (c) depicts the progression of the scattered field due to a plane wave over one period is shown below, developing in order (a→f).

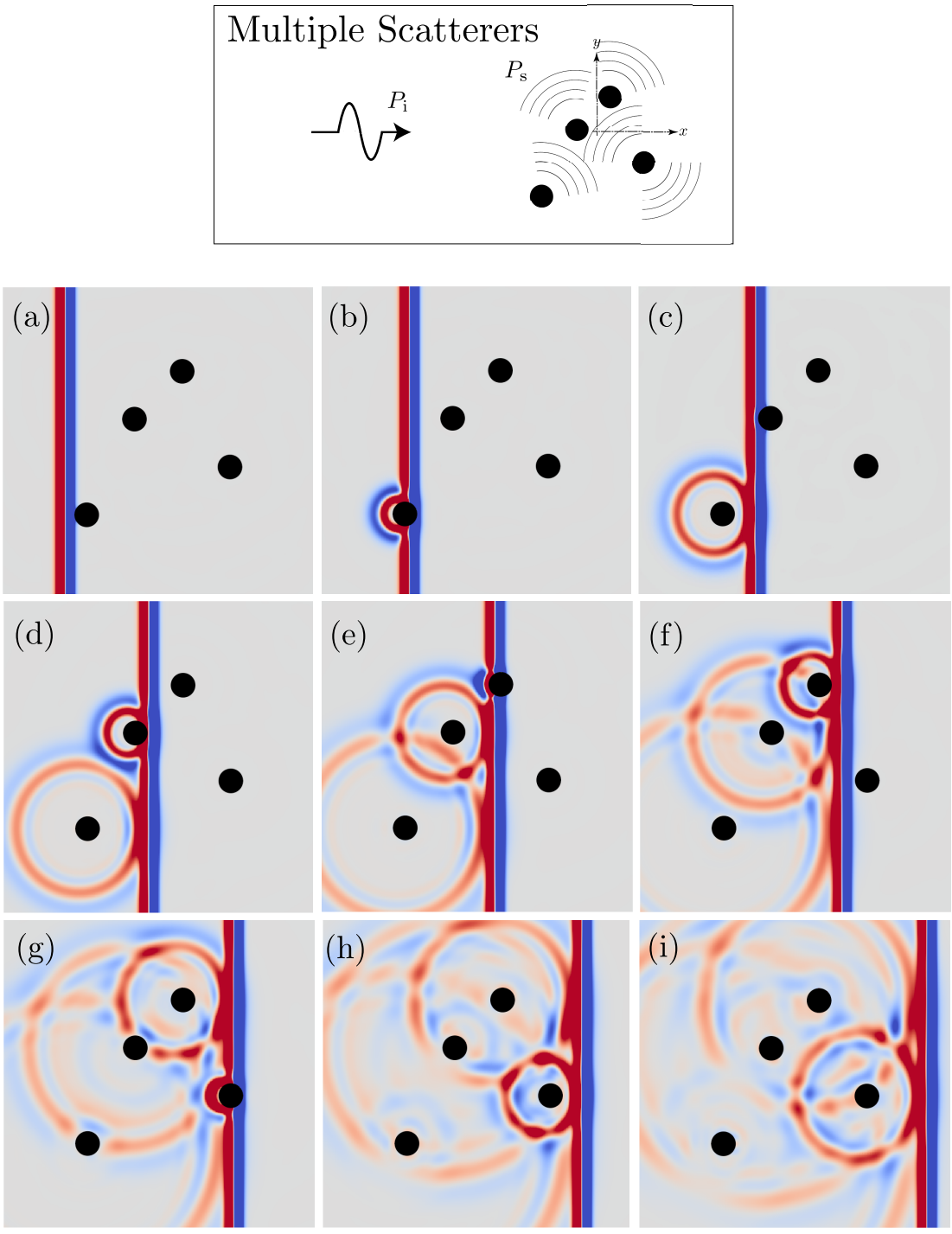

Fig. 8. An incident soliton wave impingement onto a collection of staggered cylinders. Images (a→i) illustrate the transient total acoustic field arising from primary and secondary scattering of a single wave by multiple bodies.

a leading fish in an idealized school. The wake is treated as an acoustic forcing function for the BEM described in §2, allowing observation of how the scattered acoustic field interacts in an idealized school.

An idealized model is now put forth to approximate a school of fish configuration and is used to find the scattered noise due to wake interaction in the school. A school of four fish is set into a diamond shape [25] at a distance of one chord between the fish [19]. A diamond arrangement of three static NACA 0012 airfoil cross-sections are used to define the solid boundary of the school of fish. The spacing of the fish is set to one fish length [19], at 45° from the tail of a swimmer to the follower's front. The wake generated by a fish swimming rectilinearly would not impinge on its body, allowing the replacement of the leading fish with a characteristic wake.

The characteristic wake of an individual fish is approximated here as a vortex street that would be observed downstream [4]. Two common wakes that can be observed downstream of a fish are the $2S$ wake (two single vortices per stroke cycle, also known as a reverse von Kármán vortex street) and a $2P$ wake (two pairs of vortices per stroke cycle) [24]. The strength and spacing of the vortices in the prescribed wake can be expressed as a function of the Strouhal number, $St = fA/U$, where A is the amplitude of motion, f is the frequency of tail beats, and U is the velocity. For the study, a length of 0.1 m, a velocity of 1 m/s, and an amplitude-to-length ratio of 0.2 are used to model the fish and the kinematics of the lead fish. The strength and distance of the vortices are based on these values and the Strouhal number. The strength of circulation ($\Gamma = 2\pi \tan^{-1}(\pi\ St)$), frequency ($f = U_\infty\ St/b$), and the horizontal ($a = U/f$) and vertical ($b = A$) spacings are the parameters for the study.

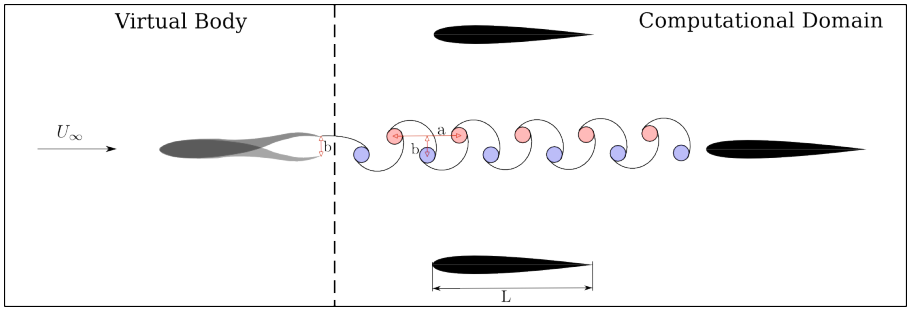

Fig. 9. A schematic of a the $2S$ vortex street interaction is shown. The leading fish is a virtual body that is replaced by the idealized vortex street. In the vortex street, blue indicates negative vorticity and red is positive vorticity. The vortex blobs in the street are spaced horizontally by distance a vertically by distance b. The fish have a length of L, which is used as the spacing between the fish.

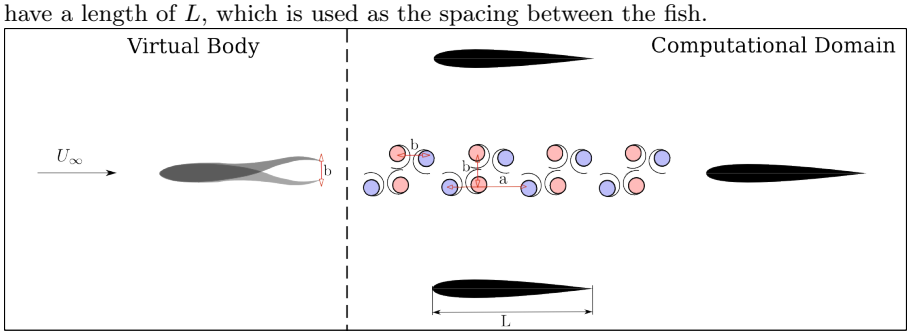

Fig. 10. A schematic of a the $2P$ vortex street interaction is shown. The virtual leading fish creates an idealized two pair, 2P, vortex street. In the vortex street, blue indicates negative vorticity and red is positive vorticity. The vortex blobs in the street are spaced horizontally by distance a vertically by distance b. The pairs of vortices are horizontally spaced by b, with each pair being the same distance from the centerline of the trailing fish. The fish have a length of L, which is also the spacing between the fish.

Figures 9 and 10 show the setup of the frozen $2S$ and $2P$ vortex streets as they advect linearly with the free stream past the other idealized fish. Vorticity in a vortex core is represented by a radially symmetric Gaussian blob. The Biot-Savart law is applied to determine velocity components for each of the vortices, yielding [3]:

$$u(\mathbf{x},t) = \sum_{i=1}^{N} \frac{-x'\ \Gamma_i}{2\pi r^2} \left(1 - \exp\left(\frac{-r^2}{2r_{\text{cut}}^2}\right)\right), \tag{24}$$

$$v(\mathbf{x},t) = \sum_{i=1}^{N} \frac{x\ \Gamma_i}{2\pi r^2}\left(1 - \exp\left(\frac{-r^2}{2r_{\text{cut}}^2}\right)\right), \tag{25}$$

where $r_{\text{cut}} = \Delta t U_\infty$ is the cut-off radius of the blobs, Γ is the circulation of the vortex blob, and $r = x^2 + x'^2$ [15]. The time step is chosen to ensure the core of a vortex does not intersect the solid geometry. At each time step the velocity induced by the vortices is defined by the Biot-Savart law. The velocities induced by the vortex street are then used as the boundary condition to the BEM formulation in §2. The motion of the vortices are idealized, as a more realistic model would feature vortex motions that are directly influenced by the flow induced by each of the rigid bodies.

The limitations of the present numerical approach are listed here. The vortex street is defined and then translated at fixed speed over the idealized school of fish. Therefore, the dynamical interaction between the vortices and bodies is neglected. The numerical model also neglects several potential acoustic features that would be found in an actual school of fish. The most notable of these features is the lack of a background flow, which would generate a boundary layer and subsequent trailing-edge noise as well as require a Kutta condition and a wake behind swimmers, which would affect the overall school noise signature.

The system of foils is subject to an semi-infinite vortex street, that starts and ends at $\pm 15 U_\infty \Delta t$ from the front and back of the school of fish. This ensures that the end of the vortex street does not have an effect on the velocity induced onto the bodies, allowing the school to reach a steady state. Each of the foils, acting as a proxy to a fish, is approximated by 4096 boundary elements. A series of 16 vortex pairs are allowed to pass through the system. Each period, $1/f$, is discretized with 32 equidistant time steps.

When a steady state is achieved, a time-average of the acoustic intensity is determined by

$$< I >= \frac{1}{T}\int_0^T \frac{|p(\tau)|^2}{\rho c} d\tau, \tag{26}$$

where T is the period of a passing $2S$ or $2P$ vortex system, corresponding to a cycle of fish tail motion.

The increasing circulation does not necessarily correspond to a greater intensity, as can be seen in figure 11. Figure 11 plots an average intensity that is scaled by the square of the circulation , with the $2P$ being scaled by $4\Gamma^2(St)$ as the system has twice as much circulation per pair. The $2S$ system shows a decreasing intensity as the Strouhal number rises, while the $2P$ system shows a maximum intensity for $St \approx 0.2$. The $2P$ street configuration initially has a lower intensity than the $2S$, then it rises to a maximum intensity at $St \approx 0.2$, before decreasing as the Strouhal number increases similar to the $2S$ street. A plateau of acoustic intensity is seen for the $2S$ street for $0.3 < St < 0.4$ in figure 11, where the $2P$ street has a slightly greater intensity than the $2S$ counterpart. A similar, but not as prominent, plateau is seen for the $2P$ street configuration in the range of $0.3 < St < 0.4$. The observation of an intensity plateau for that range of Strouhal numbers is interesting as this is the regime of Strouhal numbers where efficient swimming typically occurs. A rapid decrease for both street configurations is observed for $St > 0.4$, which is outside of the Strouhal range of what is generally considered an efficient swimmer [4].

Figure 12 shows an example of a near-field scattered pressure field of a $2S$ wake interacting with the foil arrangement at $St = 0.3$, which is a common wake structure and Strouhal number observed in swimming fish. The definition of prescribed circulation results in increasing values with increasing Strouhal number. The bottom row of figure 12 show the directivity of the average acoustic intensity for the $2S$ and $2P$ streets over the range of Strouhal numbers. The directivity is measured at 10 fish lengths from the center of the school. The $2S$ vortex streets are dominated by forward scattering of noise, which decreases as the Strouhal number increases. For intermediate Strouhal numbers, $(0.275 < St < 0.325)$, a many-lobed directivity pattern is observed. The pattern is created when the middle two foils scatter the pressure wave as it propagates from the rear foil. Figure 12 (b→ d) shows directivity plots for different ranges of Strouhal number where it can be observed that there is a switch from a front scattering to a backward scattering pattern as the Strouhal number increases. Although these are only idealized results that neglect some noise sources, further investigations into the noise production of fish could help to deepen our knowledge of predator/prey interactions. If predators swim at higher Strouhal numbers, $(St > 0.35)$, they could scatter noise backwards, effectively making them silent to any prey in front of them. In addition, the field in front the predator would be less polluted by noise scattered off of their own body, making the back scattered noise of low Strouhal number swimmers easier to detect. Similarly, these directivity patterns could be used in the design of silent bio-inspired underwater vehicles. Modulating the Strouhal number of swimming a school of bio-robotic devices could dramatically alter their sound directivity from forward to back scattering, providing a silent region behind or in front of the device.

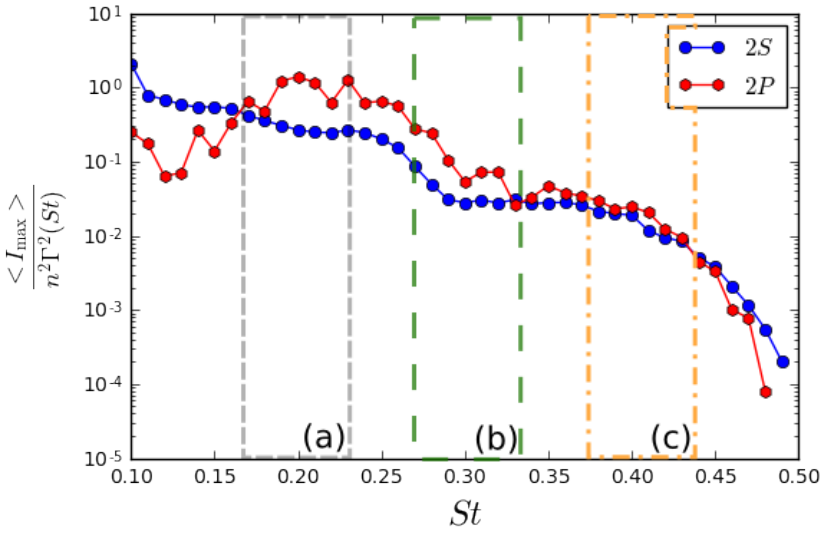

Fig. 11. A scaled maximum intensity for a range of Strouhal numbers are shown for a Strouhal range, $0.1 < St < 0.5$. The scaling is $n^2\Gamma^2(St)$, with $n = 1$ for the $2S$ street and $n = 2$ for the $2P$ street. The average intensity is found after steady-state is reached. Three sections of the plot are labeled (b $\rightarrow$ d) , which correspond to the directivity plots of figure 12.

5 Conclusions

This chapter presents a rapid transient, two-dimensional acoustic boundary element method based upon a double-layer formulation developed to examine the sound field produced by idealized vortex wakes of schooling fish. The resulting time-domain solver is validated and demonstrated to predict the scattered noise and the acoustic interaction between several rigid bodies. The time-domain boundary element method was accelerated with a fast multipole method to enable rapid evaluation of the acoustic field interactions generated by many bodies.

The boundary element method is further applied to examine the sound produced by an idealized school of fish. The wake of a virtual leader fish is fixed and moved past a formation of three rigid, static foils (fish) in the absence of a background mean flow. The simplified model presented demonstrates how the leading-edge noise of an idealized school varies over a range of Strouhal numbers that are typical of swimming fish. The directivity of the noise has a large variation within the range of Strouhal numbers examined. At lower Strouhal numbers ($0.1 < St < 0.25$) a forward scattering of the wake dominates the field while the directivity pattern transitions to a back scattering pattern for higher Strouhal numbers ($St > 0.3$). The acoustic intensity decreases as the Strouhal number increases for the $2S$ street configurations, with a similar pattern for $2P$ streets occurring after a maximum intensity is found at $St \approx 0.2$. The Strouhal range of $0.3 < St < 0.4$, commonly considered part of the range of efficient swimming, exhibits a plateau of acoustic intensity. Outside of the range of efficient swimming a sharp decrease in acoustic intensity is observed. Future work will examine the impact of a background flow, the formation of unsteady wakes from the swimmers, and the three-dimensionality and viscous effects of the flow.

References

1. Alvarez, A., Ye, Z.: Effects of fish school structures on acoustic scattering. ICES Journal of Marine Science **56**(3), 361–369 (1999)
2. Banjai, L., Sauter, S.: Rapid solution of the wave equation in unbounded domains. SIAM Journal of Numerical Analysis **7**, 227–249 (2011)
3. Cottet, G.H., Koumoutsakos, P.D.: Vortex methods: theory and practice. Cambridge University Press (2000)
4. Eloy, C.: Optimal strouhal number for swimming animals. Journal of Fluids and Structures **30**, 205–218 (2012)
5. Fay, R.R.: Fish bioacoustics. Springer (2009)
6. Feuillade, C., Nero, R., Love, R.: A low-frequency acoustic scattering model for small schools of fish. The Journal of the Acoustical Society of America **99**(1), 196–208 (1996)

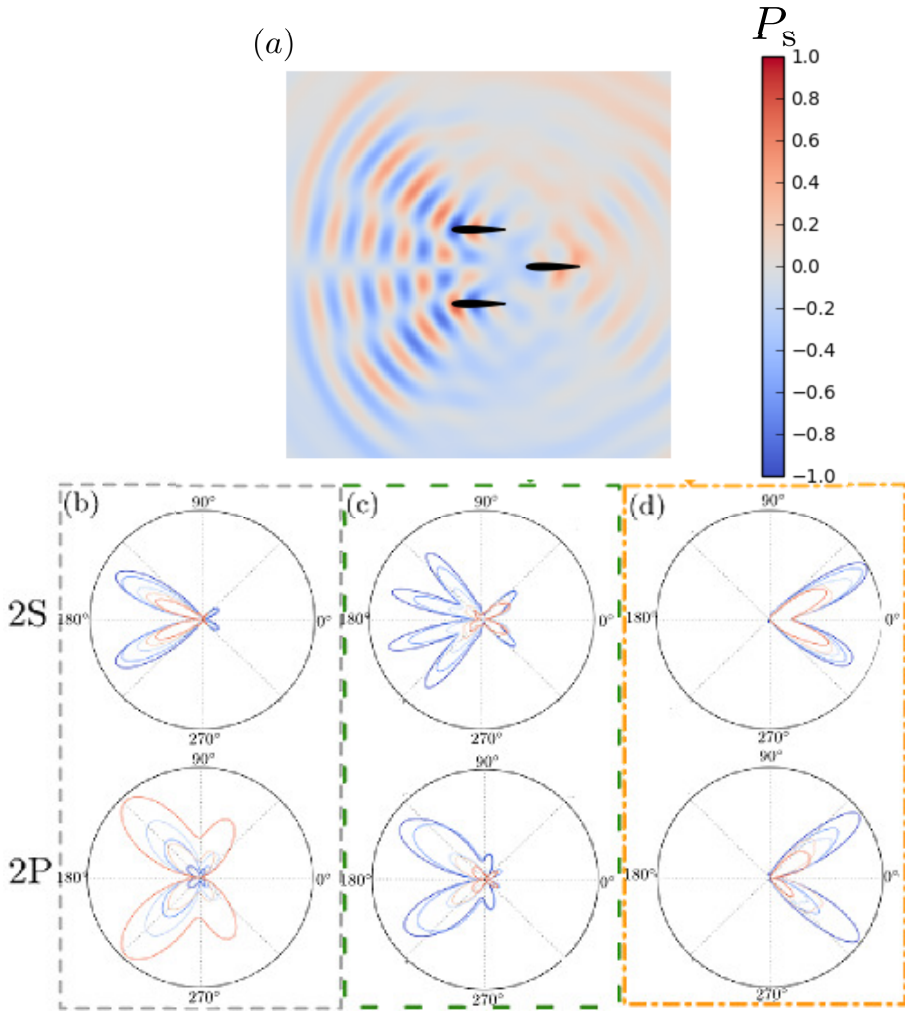

Fig. 12. The near-field scattered pressure of a $2S$ street with $St = 0.3$ is shown in image (a). The bottom row of images show the changing intensity directivity patterns for varying Strouhal number ranges. The top directivity plot is for $2S$ vortex streets and the bottom is for $2P$ vortex streets. Image (b) is for $0.175 < St < 0.225$, (c) is for $0.275 < St < 0.325$, and (d) is for $0.375 < St < 0.425$. Three sections of the plot are labeled (b $\rightarrow$ d) , which correspond to the regions of the intensity plot in figure 11.

7. Fish, F., Lauder, G.: Passive and active flow control by swimming fishes and mammals. Annu. Rev. Fluid Mech. **38**, 193–224 (2006)
8. Gimbutas, Z., Greengard, L.: FMMLIB2D, FORTRAN libraries for fast multiple method in two dimensions (2012). URL http://www.cims.nyu.edu/cmcl/fmm3dlib/fmm3dlib.html
9. Greengard, L., Rokhlin, V.: A fast algorithm for particle simulations. Journal of Computational Physics **73**(2), 325–348 (1987)
10. Hassell, M., Sayas, F.J.: Convolution quadrature for wave simulations. In: Numerical Simulation in Physics and Engineering, pp. 71–159. Springer (2016)
11. Junger, M.C., Feit, D.: Sound, structures, and their interaction, vol. 225. MIT press Cambridge, MA (1986)
12. Kirkup, S.M.: The boundary element method in acoustics. Integrated Sound Software (2007)
13. Ladich, F., Fine, M.L.: Sound-generating mechanisms in fishes: a unique diversity in vertebrates. Communication in fishes **1**, 3–43 (2006)
14. Lauder, G.V.: Fish locomotion: recent advances and new directions. Annual review of marine science **7**, 521–545 (2015)
15. Leonard, A.: Vortex methods for flow simulation. Journal of Computational Physics **37**(3), 289–335 (1980)
16. Liu, Y.: Fast multipole boundary element method: theory and applications in engineering. Cambridge University Press (2009)
17. Lubich, C.: Convolution quadrature revisited. BIT Numerical Mathematics **44**, 503–514 (2004)
18. Moored, K.W., Fish, F.E., Kemp, T.H., Bart-Smith, H.: Batoid fishes: inspiration for the next generation of underwater robots. Marine Technology Society Journal **45**(4), 99–109 (2011)
19. Partridge, B.L.: The structure and function of fish schools. Scientific american **246**(6), 114–123 (1982)
20. Raveau, M.P., Feuillade, C.: Time domain investigations of acoustical scattering from schools of swim bladder fish. The Journal of the Acoustical Society of America **135**(4), 2177–2177 (2014)
21. Read, D.A., Hover, F., Triantafyllou, M.: Forces on oscillating foils for propulsion and maneuvering. Journal of Fluids and Structures **17**(1), 163–183 (2003)
22. Rokhlin, V.: Rapid solution of integral equations of scattering theory in two dimensions. Journal of Computational Physics **86**, 414–439 (1990)
23. Saad, Y., Schultz, M.H.: GMRES: A generalized minimal residual algorithm for solving nonsymmetric linear systems. SIAM Journal on Scientific and Statistical Computing **7**(3), 856–869 (1986)
24. Schnipper, T., Andersen, A., Bohr, T.: Vortex wakes of a flapping foil. Journal of Fluid Mechanics **633**, 411–423 (2009)
25. Weihs, D.: Hydromechanics of fish schooling. Nature **241**(5387), 290–291 (1973)